Journal of Materials Chemistry B

RSC Publishing

PAPER

View Article Online
View Journal | View Issue

Cite this: *J. Mater. Chem. B*, 2013, **1**, 1279

Magnetic mesoporous bioactive glass scaffolds: preparation, physicochemistry and biological properties

Yufang Zhu,*[a] Fangjian Shang,[a] Bo Li,[a] Yu Dong,[a] Yunfei Liu,[b] Martin R. Lohe,[c] Nobutaka Hanagata[d] and Stefan Kaskel[c]

Received 17th October 2012
Accepted 2nd January 2013

DOI: 10.1039/c2tb00262k

www.rsc.org/MaterialsB

The magnetic 10Fe5Ca MBG scaffolds (Fe_3O_4–CaO–SiO_2–P_2O_5 system) have been prepared by a combination of polyurethane sponge and P123 as co-templates and an evaporation-induced self-assembly (EISA) process through the substitution of Fe_3O_4 for CaO in the 15Ca MBG scaffolds (CaO–SiO_2–P_2O_5 system). The structure, magnetic heating, drug release, physicochemical and biological properties were systematically investigated. The results showed that the 10Fe5Ca MBG scaffolds had the interconnected macroporous structure with pore sizes ranging from 200 to 400 μm and the mesoporous wall with a peak pore size of *ca.* 3.34 nm. Also, the 10Fe5Ca MBG scaffolds exhibited similar mechanical strength, apatite-forming ability and sustained drug release behavior compared to the 15Ca MBG scaffolds. Importantly, the substitution of Fe_3O_4 for CaO in the MBG scaffolds induced a slower ion dissolution rate and more significant potential to stabilize the pH environment, and facilitated osteoblast cell proliferation, alkaline phosphatase (ALP) activity and osteogenic expression. In particular, the 10Fe5Ca MBG scaffolds could generate heat in an alternating magnetic field. Therefore, the magnetic 10Fe5Ca MBG scaffolds have potential for the regeneration of the critical-size bone defects caused by bone tumors by a combination of magnetic hyperthermia and local drug delivery therapy.

Introduction

In general, critical-sized bone loss/defects caused by bone tumors cannot be repaired by physiological regenerative processes. The current orthopaedic practice for critical-sized bone defects is to use autologous bone grafts, bone allografts, or synthetic graft materials.[1] Among them, synthetic scaffolds mimicking the three-dimensional (3D) tissue structure have been considered as the most promising solutions, because an ideal 3D scaffold with a highly interconnected macroporous network facilitates cell migration, proliferation, nutrients delivery, bone ingrowth and eventually vascularization.[2–4] However, after the removal of bone tumors, the malignant cells can remain around the tumor site, leading to tumor recurrence, with fatal consequences.[5] In order to solve this problem, 3D porous scaffolds that can induce bone regeneration and at the same time destroy the tumor cells are desired.

To date, many efforts have been made to develop novel biomaterials combining bone regeneration and cancer therapy.[6–19] One of the most popular strategies is to prepare magnetic biomaterials with hyperthermia therapy, such as magnetic bioactive glass ceramics, CaP ceramics and composites.[6–15] These magnetic biomaterials implanted in the diseased tissue region can locally generate heat to raise the temperature of the surrounding when they are exposed to an alternating magnetic field. When the temperature rises to 42–45 °C, the tumor cells perish while the healthy ones survive.[16] It has been considered as an effective treatment for malignant tumors without adverse side effects.[15] However, if some tumor cells have migrated to a site far from the bone defect, magnetic hyperthermia may not kill them. Another strategy to treat bone tumor is the local drug delivery using biomaterials, in which drug is efficiently released at the diseased site to either interact with tumor cells or stimulate bone healing.[17–19] For example, Kunieda *et al.* developed the anticancer doxorubicin containing hydroxyapatite (DOX–HAP) complex to treat hepatic cancer; the slow DOX release from the DOX–HAP complex inhibited the VX2 liver tumor growth.[17] However, it requires that the biomaterials with local drug delivery should exhibit a controlled/sustained drug release behavior. Otherwise, healthy cells are often killed when the biomaterials release too high drug doses. Therefore, it is very important to develop the controlled/sustained drug delivery from biomaterials, especially from 3D porous scaffolds.

[a]*School of Materials Science and Engineering, University of Shanghai for Science and Technology, 516 Jungong Road, Shanghai, 200093, China. E-mail: zjf2412@163.com; Fax: +86-21-55270632; Tel: +86-21-55271663*

[b]*College of Materials Science and Engineering, Nanjing University of Technology, 5 Xinmofan Road, Nanjing, 210009, China*

[c]*Professur für Anorganische Chemie I, Fachrichtung Chemie und Lebensmittelchemie, Technische Universität Dresden, Bergstrasse 66, Dresden, 01062, Germany*

[d]*Interdisciplinary Laboratory for Nanoscale Science and Technology, National Institute for Materials Science, 1-2-1 Sengen, Tsukuba, Ibaraki, 305-0047, Japan*

Obviously, the development of 3D porous scaffolds combining magnetic hyperthermia and the controlled/sustained local drug delivery would be desired to repair the critical-sized bone defects caused by bone tumors. However, it is still a significant challenge to prepare the ideal scaffolds to meet the multifunctionality.

Recently, mesoporous bioactive glasses (MBGs), such as the $CaO–SiO_2–P_2O_5$ system, have received much interest in bone tissue regeneration and drug delivery.[20–31] The MBGs have high surface area, large pore volume and mesoporous structure, which results in an enhanced bone-forming bioactivity compared to the conventional bioactive glasses (BGs),[20–28] and they can also effectively load drugs, such as antibiotics or growth factors, as a potential local drug delivery system.[29–31] On the other hand, the composition of MBGs can be easily incorporated or substituted by using the sol–gel method. We have successfully substituted ZrO_2, MgO and SrO for CaO in the $CaO–SiO_2–P_2O_5$ MBG scaffolds to enhance the physicochemical and biological properties.[32,33] Wu *et al.* have reported the boron, strontium and cobalt-containing $CaO–SiO_2–P_2O_5$ MBG scaffolds for bone tissue engineering.[34–36] Salinas *et al.* have demonstrated the substitutions of cerium, gallium and zinc in MBGs for the enhancement of physiological functions.[37] Therefore, it is believed that magnetic MBG scaffolds could be prepared by the incorporation or substitution of magnetic components in the MBG scaffolds. Thus, the preparation of 3D magnetic MBG scaffolds could combine the bone regeneration, magnetic hyperthermia and controlled local drug delivery for repairing the critical-size bone defects caused by bone tumors. To date, only Wu *et al.* have prepared the Fe-incorporating MBG scaffolds for bone regeneration by combining the functions of drug delivery and hyperthermia.[38] However, the calcination treatment at 700 °C under an air atmosphere induced the formation of α-Fe_2O_3 in the MBG scaffolds, which resulted in very weak magnetization of the Fe-MBG scaffolds. Therefore, it is still a challenge to develop the multifunctional 3D magnetic MBG scaffolds for repairing the critical-size bone defects caused by bone tumors.

In this study, we reported the preparation of magnetic MBG scaffolds ($Fe_3O_4–CaO–SiO_2–P_2O_5$ system) by the combination of polyurethane sponge and P123 as co-templates and an evaporation-induced self-assembly (EISA) process. Using $CaO–SiO_2–P_2O_5$ MBG scaffolds as a control due to their potential for bone regeneration as new bioactive biomaterials,[32–38] the structure, magnetic heating, and physicochemical and biological properties were systematically investigated. Gentamicin, a wide spectrum antibiotic treating osteomyelitis, was selected as the model drug and introduced into the magnetic MBG scaffolds to obtain a sustained local drug delivery system.

Experimental methods

Preparation and characterization of magnetic MBG scaffolds

Magnetic MBG scaffolds were prepared following our previously reported method after some modification.[32] In a typical synthesis, 4.0 g of P123 ($M_w = 5800$, Aldrich), 6.7 g of tetraethyl orthosilicate (TEOS, 98%, Acros), 0.47 g of calcium nitrate ($Ca(NO_3)_2 \cdot 4H_2O$), 1.08 g of ferric chloride hexahydrate ($FeCl_3 \cdot 6H_2O$), 0.73 g of triethyl phosphate (TEP, 99.8%, Sigma-Aldrich) and 1.0 g of 0.5 M HCl were dissolved in 60 g of ethanol, and stirred at room temperature for 1 day (molar ratio of Fe : Ca : Si :P = 10 : 5 : 80 : 5). Afterwards, the polyurethane sponges were completely immersed into the sol for 10 min, and transferred to a Petri dish to squeeze out the excess sol. After evaporating the solution for 12 h at room temperature, the same procedure was repeated 8 times. When the samples were completely dry, they were calcined at 700 °C (ramp of 2 °C min^{-1}) for 8 h, and then reduced in 10% H_2/90% Ar at 400 °C for 3 h to obtain magnetic MBG scaffolds, named as the 10Fe5Ca MBG scaffolds. The $CaO–SiO_2–P_2O_5$ MBG scaffolds (molar ratio of Ca : Si : P = 15 : 80 : 5) were prepared according to the previously reported method, named the 15Ca MBG scaffolds.[23]

The small angle X-ray diffraction (SAXRD) patterns were measured on a Bruker AXS Nanostar using CuKα_1 radiation (1.5405 Å) and a sample to detector distance of 105 cm. The wide angle X-ray diffraction (WAXRD) patterns were obtained on a Stoe Stadi P powder diffractometer equipped with a curved germanium (111) monochromator and linear PSD using Cu Kα_1 radiation (1.5405 Å) in transmission geometry. Scanning electron microscopy (SEM) was carried out with a JSM-7001F field emission scanning electron microscope. Transmission electron microscopy (TEM) was performed with a JEM-2010 UHR electron microscope operated at an acceleration voltage of 200 kV. N_2 adsorption–desorption isotherms were obtained on a Micromeritics Tristar 3000 pore analyzer at −196 °C under the continuous adsorption condition. Brunauer–Emmett–Teller (BET) and Barrett–Joyner–Halenda (BJH) methods were used to determine the surface area, the pore size distribution and the pore volume. Magnetic measurement was performed using a vibrating sample magnetometer (VSM).

Porosity and mechanical strength of magnetic MBG scaffolds

The porosity of magnetic MBG scaffolds was measured using the Archimedes principle: magnetic MBG scaffolds with a size of 7 × 7 × 7 mm were used for the measurement and water was used as the liquid medium. The porosity (P) was calculated according to the following formulation $P = (W_{sat} - W_{dry})/(W_{sat} - W_{sus}) \times 100\%$, where W_{dry} is the dry weight of magnetic MBG scaffolds, W_{sus} is the weight of magnetic MBG scaffolds suspended in water, and W_{sat} is the weight of magnetic MBG scaffolds saturated with water.

The compressive strength of the 7 × 7 × 7 mm sized magnetic MBG scaffolds were tested using a TA.XT2i texture analyser (Stable Micro System) at a cross head speed of 0.5 mm min^{-1}.

Ion dissolution and apatite formation of magnetic MBG scaffolds in simulated body fluids

To investigate the ion dissolution from magnetic MBG scaffolds, simulated body fluids (SBF) were prepared and buffered at pH 7.4 with tris(hydroxymethyl)aminomethane [$(CH_2OH)_3CNH_2$] and hydrochloric acid (HCl) according to Kokubo's method.[39] Magnetic MBG scaffolds were soaked in SBF solutions at 37 °C for 1, 3, 5 and 7 days, and the ratio of the

SBF volume to the scaffold mass was 200 ml g^{-1}. The Si, Ca, P and Fe ions in SBF solutions were determined by an inductively coupled plasma optical emission spectrometer (ICP-OES, Shimadzu ICPS-8100). The pH values of SBF solutions were tested after soaking the magnetic MBG scaffolds at the predetermined time intervals.

The apatite formation ability of magnetic MBG scaffolds was also carried out in SBF solutions. Generally, 0.1 g of magnetic MBG scaffolds was soaked in 20 ml of SBF solution in a polyethylene bottle at 37 °C for different periods. After soaking, magnetic MBG scaffolds were collected from the SBF solution, rinsed with ethanol and dried. SEM observation was used to study the apatite formation on the surfaces of magnetic MBG scaffolds.

Magnetic heating property of magnetic MBG scaffolds

For the magnetic heating experiment, a TruHeat HF 5005 high frequency generator from Hüttinger Elektronik was used. The used inductor was a water-cooled copper coil with 11 turns on a length of 105 mm and a diameter of 42.5 mm. For measurement, an open topped vessel with a dispersion of magnetic MBG particles ground from the scaffolds was placed in the inductor. During application of the alternating magnetic field, the temperature was monitored using a pyrometer that was placed above the inductor and focused on the dispersion surface. To obtain the heating curve of the magnetic MBG scaffolds, a reference measurement of the pure solvent (equivalent volume) was subtracted from the data.

Cell culture

Osteoblast-like cells, MC3T3-E1, were used to assay the osteoblast responses on magnetic MBG scaffolds. Culture for cell proliferation was conducted at 37 °C in a humidified 5% CO_2 atmosphere in a proliferation medium consisting of α-Modified Eagle's Medium (α-MEM) with 10% (v/v) fetal bovine serum (FBS), 100 U ml^{-1} penicillin, and 100 μg ml^{-1} streptomycin. Culturing for cell differentiation was conducted at 37 °C in a humidified 5% CO_2 atmosphere in a differentiation medium, which is a proliferation medium supplemented with 2 mmol l^{-1} β-glycerophosphate. The medium was changed every 3 days.

Proliferation of MC3T3-E1 cells on magnetic MBG scaffolds

Cell proliferation was measured by the MTT (3-(4,5-dimethylthiazol-2-yl)-2,5-diphenyltetrazolium bromide) method. Briefly, the MBG scaffolds were placed into 24-well culture plates. 1×10^5 MC3T3-E1 cells in a 60 μl suspension were placed onto each scaffold and allowed to adhere to magnetic MBG scaffolds for 3 h, after which the cell–scaffold complexes were covered with 1.2 ml of proliferation medium. The cells were incubated for 1, 3 and 7 days at 37 °C in a humidified 5% CO_2 atmosphere. At 1, 3 and 7 days, the MBG scaffolds were washed 3 times with PBS. Subsequently, 1.0 ml of 0.5 mg ml^{-1} MTT solution was added into each well and incubated for 4 h at 37 °C. After the removal of MTT solution by the adsorption with dry papers, the MBG scaffolds were transferred to 1.5 ml tubes, and 500 μl of dimethyl sulfoxide (DMSO) was added to each tube. After formazan was dissolved completely into DMSO, 100 μl of formazan solution was transferred to 96-well plates and the absorbance was recorded using a microplate reader (MTP-880, Corona) at 492 nm. The results were expressed as the absorbance reading from each well minus the optical density (OD) value of a blank.

Alkaline phosphatase (ALP) activity of MC3T3-E1 cells on magnetic MBG scaffolds

The osteogenic differentiation was assessed by measuring a time course of alkaline phosphatase (ALP) activity of MC3T3-E1 cells grown on magnetic MBG scaffolds. The magnetic MBG scaffolds were placed into 24-well plates and seeded with 1×10^5 cells per scaffold. The cells were cultured for 4 days with a proliferation medium, and followed for 5, 10 and 15 days with a differentiation medium. At 5, 10 and 15 days, the samples were removed and ALP activity was measured. The scaffolds were irrigated with 0.9% NaCl solution three times to remove as much residual serum as possible and then 100 μl of 0.1% Triton® X-100 in 0.9% NaCl solution was used to dissolve the cells on the scaffold for 15 min at room temperature. Subsequently, the samples were centrifuged at 10 000 × *g* at 4 °C for 1 min, and the supernatant transferred to fresh 1.5 ml tubes for ALP activity measurement using a LabAssay™ ALP Kit (Wako, Japan) according to the manufacturer's instructions. Typically, 50 μl of substrate buffer and 10 μl of the sample supernatant were mixed and incubated for 30 min at 37 °C, and then the reaction was stopped by the addition of 40 μl of stop solution. Using *p*-nitrophenol as a standard solution, the optical density was measured at 415 nm with a microplate reader (MTP-880, Corona). The ALP activity was calculated from a standard curve after normalizing to the total protein content, which was measured using a Pierce BCA Protein Assay Kit (Thermo Scientific) on a microplate reader (MTP-880, Corona).

Quantitative real-time PCR analysis

The osteogenic differentiation of MC3T3-E1 cells on magnetic MBG scaffolds was further assessed by quantitative Real-Time PCR (RT-PCR) to measure the mRNA expression of collagen type I (Colla1), bone gamma-carboxyglutamate protein 2 (Bglap2) and interferon induced transmembrane protein 5 (Ifitm5). The magnetic MBG scaffolds were placed in 24-well plates and a total of 1×10^5 cells were seeded onto each scaffold. The cells were cultured for 4 days with a proliferation medium, and followed for 5, 10 and 15 days with a differentiation medium. At 5, 10 and 15 days, the samples were removed and total RNA was extracted using Isogen solution (Wako, Japan) and treated with a DNase I digestion step according to the manufacturer's instructions. The concentration level of the RNA was determined on a NanoDrop 2000 spectrophotometer (Thermo Scientific) at 260 nm. Single-strand cDNA was synthesized from 500 ng of total RNA using a PrimeScript™ RT reagent Kit (Takara, Japan) following the manufacturer's instructions. The cDNA was analyzed for markers of osteogenic differentiation: Colla1, Bglap2 and Ifitm5. Glyceraldehyde 3-phosphate dehydrogenase (Gapdh) was utilized as a reference. Primers for the

Table 1 Primers used for RT-PCR-MC3T3-E1 cells related markers

Gene	Forward primer	Reverse primer
Gapdh	GTGGACCTCATGGCCTACAT	TGTGAGGGAGATGCTCAGTG
Colla1	CAGCTCCTGGGAGTTACAGC	AAGTGGGGAAAGGGACAAAG
Bglap2	CAGTCGCTTCACCTACAGCA	GGTGGAGGGAGTTTACACGA
Ifitm5	AAGCAGGAGGGCAATAAGGT	TTTGTAGGCGGTCTTCAAGC

selected genes are listed in Table 1. RT-PCR was performed using the LightCycler FastStart DNA Master SYBER Green I Kit (Roche Applied Science, Japan). 15 μl of reaction solution contains 1.5 μl of LightCycler Mix (Roche Applied Science, Japan), 0.75 μl each of 10 μM forward and reverse primers, 1.0 μl of cDNA template diluted 1 : 10, 0.6 μl of 25 mM $MgCl_2$ solution, and 10.4 μl of RNase free water using the LightCycler System (Roche Applied Science, Japan). Relative expression levels for each gene were normalized against the initial concentration value of the reference gene (Gapdh) and determined by using the second derivative maximum method.

Loading and *in vitro* release of gentamicin

0.5 g of magnetic MBG scaffolds was immersed in 20 ml of a gentamicin solution (10 mg ml^{-1}). After 24 h, the drug-loaded MBG scaffolds were separated and dried at room temperature for 48 h. The estimation of gentamicin loaded in magnetic MBG scaffolds was carried out by measuring the absorbance values at 256 nm before and after loading.[24] Before determination, a calibration curve was recorded.

In vitro release of gentamicin from the drug-loaded MBG scaffolds was carried out with a shaking bed at 37 °C. The drug-loaded MBG scaffold (0.2 g) was placed in a cover-sealed plastic bottle with 20 ml of SBF solution, and the plastic bottle was fixed on the shaking bed with a shaking speed of 50 ramp. Gentamicin release was determined by UV analysis. The release medium was withdrawn at the predetermined time intervals, and replaced with fresh SBF solution each time.

Statistical analysis

The statistical analysis was performed using One-Way ANOVA with a Post Hoc test. All data are expressed as means ± standard deviation ($n = 5$). Differences were considered statistically significant for $*p < 0.05$.

Results and discussion

Preparation and characterization of magnetic MBG scaffolds

SEM images of the 10Fe5Ca and 15Ca MBG scaffolds are shown in Fig. 1. It can be observed that the 10Fe5Ca MBG scaffolds has the interconnected macroporous structure with pore size ranging from 200 to 400 μm, similar to that of the 15Ca MBG scaffolds. Furthermore, the 10Fe5Ca MBG scaffolds have similar porosity compared to the 15Ca MBG scaffolds. The porosity of the 10Fe5Ca and 15Ca MBG scaffolds was estimated at 86.4% and 88.6%, respectively (in Table 2). Therefore, the 10Fe5Ca MBG scaffolds have a suitable interconnected macroporous structure for bone regeneration, because the pore size of macropores larger than 150 μm and high porosity are ideal for the scaffolds for bone regeneration, which facilitates the cell proliferation, vascular ingrowth, and internal mineralized bone formation.[4,40] The compressive strengths of the 10Fe5Ca and 15Ca MBG scaffolds were estimated to be 64.3 ± 14.9 and 52.8 ± 12.4 kPa, respectively, similar to those of HAp scaffolds (30 kPa) and β-TCP scaffolds (50 kPa).[41,42]

The WAXRD patterns of the 10Fe5Ca and 15Ca MBG scaffolds are shown in Fig. 2. A broad reflection at $2\theta = 15–35°$ associated with amorphous silicate can be seen on both WAXRD patterns. However the characteristic diffraction peaks of Fe_3O_4 corresponding to the (311), (511), and (440) reflections can be clearly observed for the 10Fe5Ca MBG scaffolds (JCPDS 75-1609) except the broad reflection indexed to amorphous silicate. It is attributed to the reduction from hematite to magnetite in the 10Fe5Ca MBG scaffolds under a H_2/Ar atmosphere. Furthermore, the component distributions of the 10Fe5Ca MBG scaffolds were evaluated by element mapping (Fig. 1D). It can be clearly observed that the chemical compositions (Ca, Fe, Si, P and O) are distributed homogeneously, which indicates that the sol–gel technique permits the synthesis of homogeneous Fe_3O_4–CaO–SiO_2–P_2O_5 magnetic MBG scaffolds.

Fig. 3 shows the SAXRD patterns of the 10Fe5Ca and 15Ca MBG scaffolds. There is an apparent diffraction peak at $2\theta = 1–1.5°$ for both MBG scaffolds, which is similar to those of previous reported MBG powders and scaffolds.[20,23] It suggested that the 10Fe5Ca MBG scaffolds have mesoporous pore walls similar to the 15Ca MBG scaffolds. However, it can be observed that the diffraction intensity and the diffraction peak position of the 10Fe5Ca MBG scaffolds show a slight decrease and a slight shift to higher angle compared to those for the 15Ca MBG scaffolds, respectively. It might be attributed to a slight decrease of the ordered degree and a slight decrease of mesopore size after the substitution of Fe_3O_4 for CaO in the MBG scaffolds.

Fig. 4 shows TEM images of the 10Fe5Ca and 15Ca MBG scaffolds. Both MBG scaffolds exhibit an ordered mesoporous structure, which is consistent with the results of the SAXRD analysis and is similar to those of the MBG powders and scaffolds.[20,23–38] However, the Fe_3O_4 particles or aggregates cannot be clearly observed in the 10Fe5Ca MBG matrix. It might be that Fe ions substitute Ca ions in the framework of the MBG scaffolds, resulting in the formation of very small Fe_3O_4 crystals after the calcination and the reduction under a H_2/Ar atmosphere. There was no significant contrast between small Fe_3O_4 crystals and silica matrix in the TEM observation.

Fig. 5 shows N_2 adsorption–desorption isotherms of the 10Fe5Ca and 15Ca MBG scaffolds together with the corresponding pore size distributions. The data for the surface area, pore volume and pore size are listed in Table 2. As shown in Fig. 5A, similar to the 15Ca MBG scaffolds, the 10Fe5Ca MBG scaffolds also exhibited the type IV isotherm and the type H1 hysteresis loop, indicating the *p6mm* mesoporous structure. However, compared to the 15Ca MBG scaffolds, the 10Fe5Ca MBG scaffolds showed a slight decrease in the N_2 adsorbed volume, which suggests that the substitution of Fe_3O_4 for CaO would slightly decrease the surface area and pore volume of the

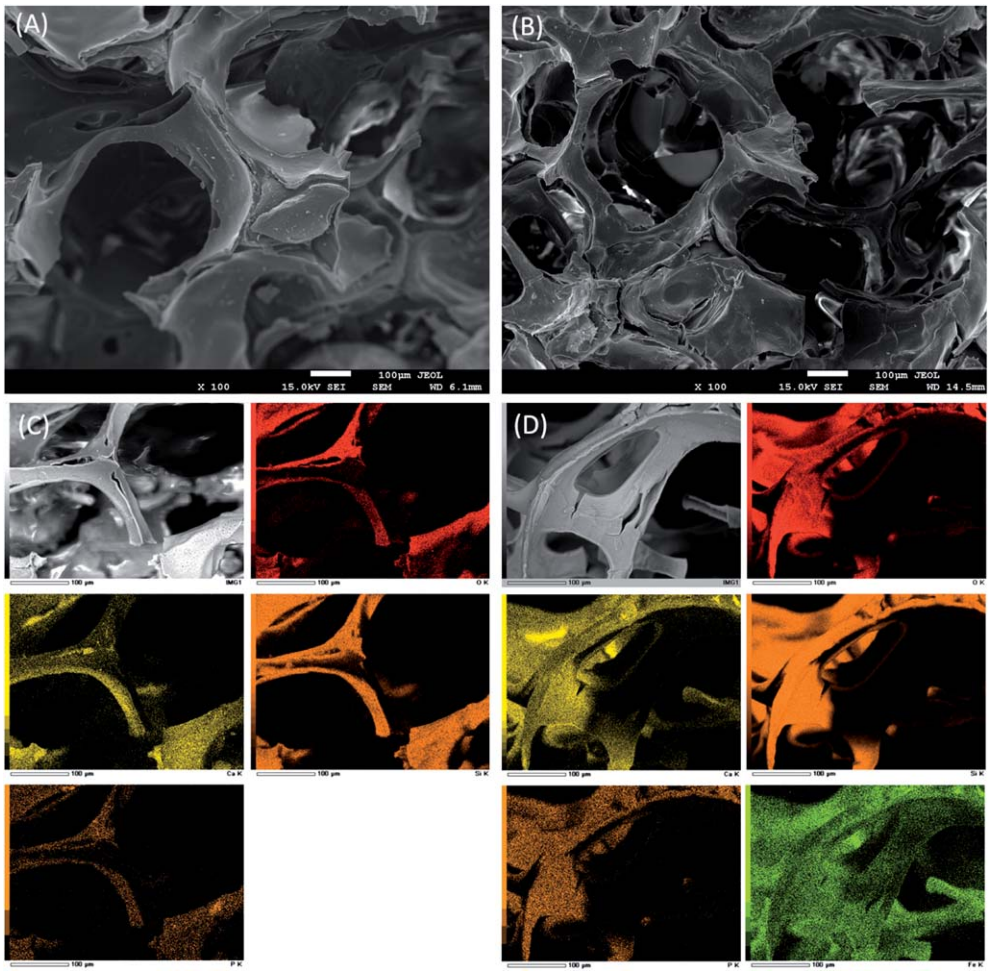

Fig. 1 SEM images (A and B) and element mappings (C and D) of the 15Ca (A and C) and 10Fe5Ca (B and D) MBG scaffolds.

MBG scaffolds. The surface areas of the 10Fe5Ca and 15Ca MBG scaffolds were 221.3 and 327.3 $m^2\ g^{-1}$, respectively. The single point adsorption total volumes at $P/P_0 = 0.98$ were 0.286 and 0.357 $cm^3\ g^{-1}$ for the 10Fe5Ca and 15Ca MBG scaffolds, respectively. It might be attributed to the decrease of the ordered degree of the 10Fe5Ca MBG scaffolds, because the substitution of Fe_3O_4 for CaO may cause defects in the mesoporous framework due to the difference of valence and atom diameter. The phenomenon can be found in the substitutions of other oxides for CaO in mesoporous materials.[32–38] The pore size distribution curves in Fig. 5B were calculated from the adsorption branches using the BJH model. The 10Fe5Ca and 15Ca MBG scaffolds presented the relatively narrow pore size distributions and the peak pore sizes were 3.34 and 4.07 nm, respectively, which is consistent with the SAXRD analysis.

It has been demonstrated that the hierarchically mesoporous–macroporous structure of the scaffolds could enhance the apatite-forming ability due to the large surface area of the MBG scaffolds resulting in high chemical reactivity.[24,43–45] Furthermore, the mesopores of the scaffold walls favor cell adhesion and adsorption of biological metabolites.[46] In this study, the Fe_3O_4–CaO–SiO_2–P_2O_5 MBG scaffolds have the interconnected macroporous network with a pore diameter of 200–400 μm and the mesoporous wall with a surface area of 221.3 $m^2\ g^{-1}$ and mesopore size of 3.34 nm. The beneficial structure may induce the Fe_3O_4–CaO–SiO_2–P_2O_5 MBG scaffolds

Table 2 Structural parameters and gentamicin loading of the MBG scaffolds

	Fe : Ca : Si : P (molar ratio)							
Samples	Theoretical value	Measured value	S_{BET} ($m^2\ g^{-1}$)	V_p ($cm^3\ g^{-1}$)	D_p (nm)	Porosity (%)	Mechanical strength (kPa)	Drug loading (%)
15Ca	0 : 15 : 80 : 5	0 : 15.8 : 79.3 : 4.9	327.3	0.357	4.07	88.6	52.8 ± 12.4	12.1
10Fe5Ca	10 : 5 : 80 : 5	9.1 : 5.5 : 80.6 : 4.8	221.3	0.286	3.34	86.4	64.3 ± 14.9	10.9

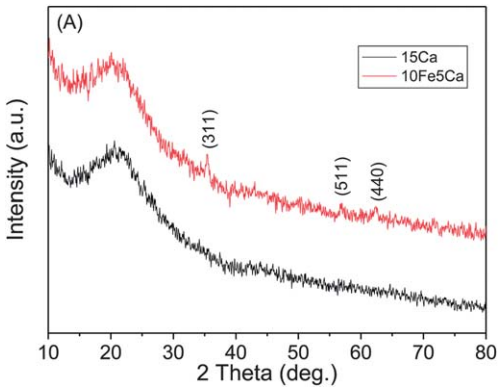

Fig. 2 The WAXRD patterns of the 15Ca and 10Fe5Ca MBG scaffolds.

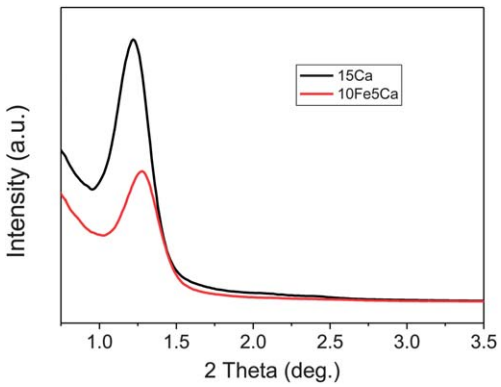

Fig. 3 The SAXRD patterns of the 15Ca and 10Fe5Ca MBG scaffolds.

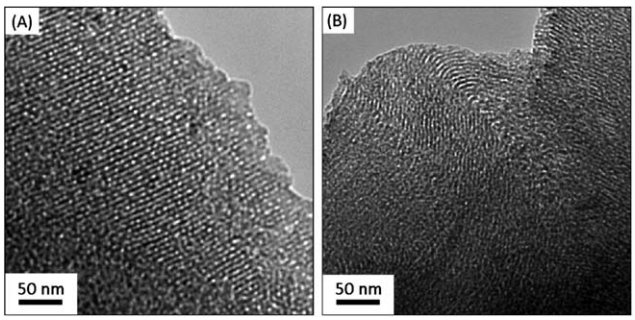

Fig. 4 TEM images of the 15Ca (A) and 10Fe5Ca (B) MBG scaffolds.

to have good apatite-forming bioactivity, cell attachment, proliferation and differentiation. Furthermore, the mesoporous structure of the scaffold walls also has the ability to deliver drugs, growth factors, antibiotics or nutrients in a controlled/sustained release manner.

Magnetic heating property of magnetic MBG scaffolds

The magnetization curve of the 10Fe5Ca MBG scaffolds at room temperature is shown in Fig. 6. The magnetization saturation (M_s) value is about 1.75 emu g^{-1}, and almost no hysteresis loop can be observed in the magnetization curve, suggesting a

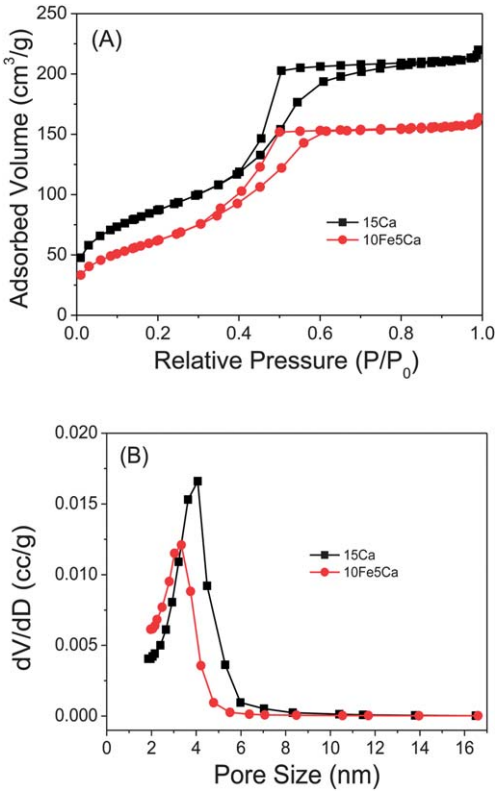

Fig. 5 N_2 adsorption–desorption isotherms (A) and the corresponding pore size distributions (B) of the 15Ca and 10Fe5Ca MBG scaffolds.

superparamagnetic property for the 10Fe5Ca MBG scaffolds. It might be attributed to the formation of very small Fe_3O_4 particles in the MBG scaffolds. The substitution of Fe_3O_4 for CaO in the MBG scaffolds by using the sol–gel technique led to the homogeneous distribution of Fe_3O_4 in the framework as shown in the element mapping of the 10Fe5Ca MBG scaffolds, which limits the Fe_3O_4 growth due to the confined effect of the framework. It is consistent with the result of the TEM observation.

Regarding the magnetic heating property of the 10Fe5Ca MBG scaffolds, Fig. 6B shows the temperature increase of the 10Fe5Ca MBG scaffolds in an alternating magnetic field whose magnetic field strength and frequency were 1.47 kA m^{-1} and 232 kHz, respectively. It can be observed that the temperature of the 10Fe5Ca suspension increased from 36 °C to 44.25 °C after measuring 25 min. In the absence of the 10Fe5Ca MBG scaffolds, the temperature in the aqueous solution experienced minimal variation, starting at 36 °C at the beginning of magnetic field application and ending at 36.5 °C after the observation period.

It has also been demonstrated that superparamagnetic materials can generate heat in an alternating magnetic field due to the delay in the Neel relaxation of the magnetic moment.[14,16] The 10Fe5Ca MBG scaffolds were superparamagnetic, allowing generation of heat under an alternating magnetic field. On the other hand, tumor cells are destroyed when they are heated to about 43 °C.[12,16] The 10Fe5Ca MBG scaffolds could generate enough heat to raise the temperature of the surrounding environment to above 43 °C. Therefore, the 10Fe5Ca MBG scaffolds could be effective heating sources in hyperthermia.

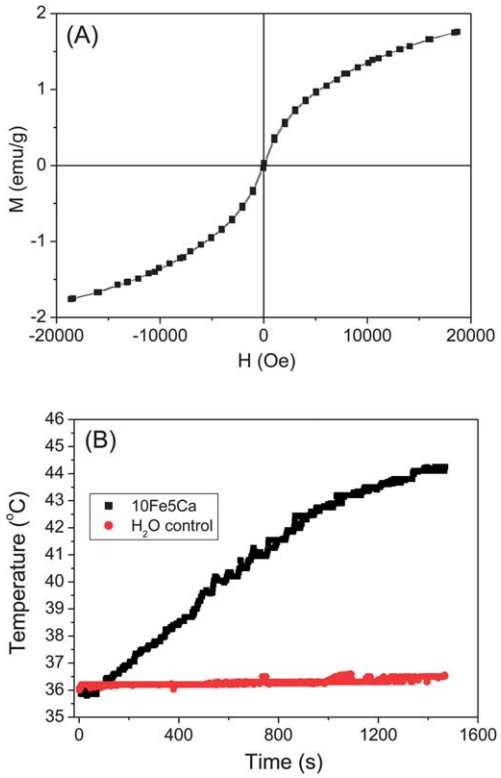

Fig. 6 (A) Magnetic curve as a function of the applied magnetic field for the 10Fe5Ca MBG scaffolds at room temperature; (B) magnetic heating curve of 200 mg 10Fe5Ca MBG scaffolds in 3 ml of H_2O at 232 kHz and a field strength of 1.47 kA m^{-1}.

Ion dissolution and apatite-forming ability of magnetic MBG scaffolds

The dissolution of ions from the scaffold biomaterials induces the pH changes in the surrounding environment, which will affect cell growth and the osseointegration ability. Also, previous studies demonstrated that many types of ions released from biomaterials, such as Ca and Si ions, can stimulate osteoblast proliferation, differentiation and gene expression, regarded as one of the evaluation criteria for bioactivity of the materials.[32,34,47] In this study, the dissolutions of Si, Ca, Fe, P ions from the MBG scaffolds and pH changes after soaking in SBF solutions were investigated. As shown in Fig. 7, the concentrations of the dissolved Si and Ca ions increased for both MBG scaffolds with increasing soaking time. Compared to the 15Ca MBG scaffolds, the 10Fe5Ca MBG scaffolds had a similar dissolution profile of Si ions, but the dissolution of Ca ions decreased due to the substitution of Fe_3O_4 for CaO. Interestingly, the concentrations of P ions in SBF solutions decreased for both MBG scaffolds with increasing soaking time in SBF solutions, which might be attributed to the apatite formation. The concentration of Fe ions for the 10Fe5Ca MBG scaffolds was <1 mg ml^{-1} (not shown), which indicates that Fe ions dissolved from the 10Fe5Ca MBG scaffolds were too less to detect accurately by ICP-OES. On the other hand, it can be observed that the pH value of SBF solution soaked with the 15Ca MBG scaffolds increased from 7.4 to 8.1 in 7 days, while that

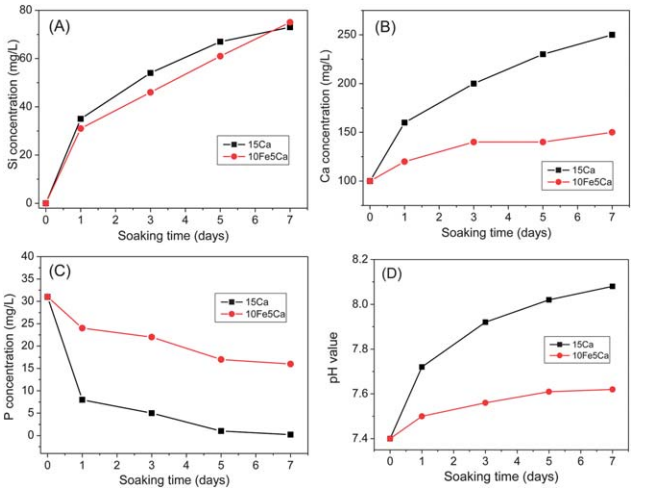

Fig. 7 Si (A), Ca (B) and P (C) concentrations in SBF solutions and pH values (D) of SBF solutions after soaking the 15Ca and 10Fe5Ca MBG scaffolds.

soaked with the 10Fe5Ca MBG scaffolds only increased to 7.6 in 7 days. It may be attributed to the significantly decreased dissolution of Ca ions and the similar dissolution of Si ions from the 10Fe5Ca MBG scaffolds compared to the 15Ca MBG scaffolds. It indicates that the 10Fe5Ca MBG scaffolds exhibited greater significant potential to stabilize the pH value in the surrounding environment compared to the 15Ca MBG scaffolds, and would be beneficial for cell adhesion and growth on the scaffolds.

The bioactive characteristic of the scaffold biomaterials is their ability to bond with living bone through the formation of an apatite layer on their surface both *in vitro* and *in vivo*.[23] It also has been demonstrated that osteoblast growth and differentiation are influenced by apatite forming on the surface of biomaterials.[39,48] Therefore, apatite-forming ability is very important for the magnetic MBG scaffolds. As shown in Fig. 8, the 10Fe5Ca and 15Ca MBG scaffolds had smooth surfaces before being soaked in SBF; however, after soaking for 3 days, microparticles were deposited on the surfaces of the scaffolds, which is similar to the previously reported formation of apatite particles on the MBG powders and scaffolds.[20,24] Furthermore, EDS analysis shows that the ratios of Ca/P were 1.78 and 1.72 for the 10Fe5Ca and 15Ca MBG scaffolds, respectively, which is close to the Ca/P ratio of hydroxyapatite (1.67). It suggests that the 10Fe5Ca and 15Ca MBG scaffolds are bioactive according to Kokubo's view.[39]

Compared to the 15Ca MBG scaffolds, the 10Fe5Ca MBG scaffolds exhibited slightly slower apatite formation rate according to the fewer apatite particles on the surface of the scaffolds. The reported mechanism of apatite formation on the silicate bioactive glass demonstrated that more Ca ions in SBF and more Si–OH groups on the silicate bioactive glass facilitate the apatite formation.[49,50] The 10Fe5Ca MBG scaffolds showed less Ca ion dissolution due to the substitution of Fe_3O_4 for CaO in the MBG scaffolds, resulting in fewer Ca ions in SBF solution, which might be contributed to the slower apatite formation rate on the 10Fe5Ca MBG scaffolds.

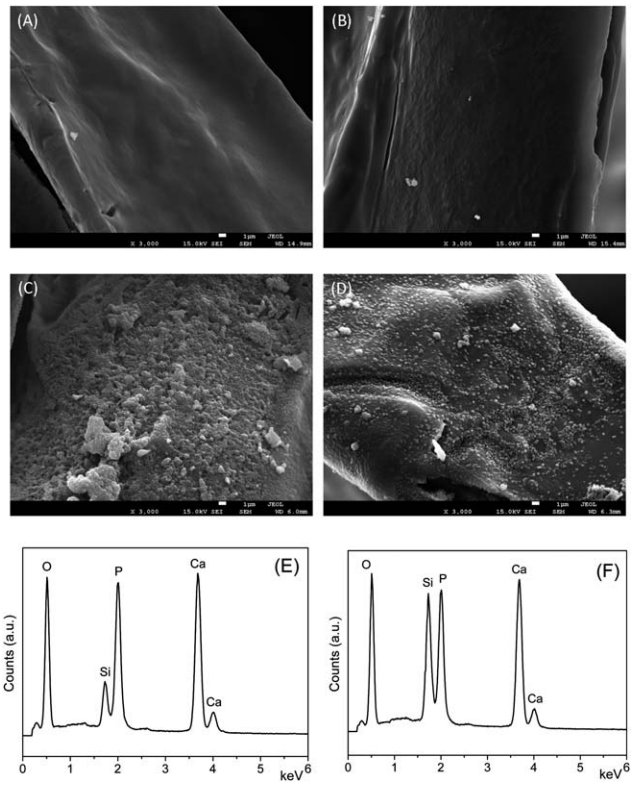

Fig. 8 SEM images of the 15Ca MBG scaffolds (A) before and (C) after, and the 10Fe5Ca MBG scaffolds (B) before and (D) after soaking in SBF solutions for 3 days; EDS analysis of the 15Ca (E) and 10Fe5Ca (F) MBG scaffolds after soaking in SBF solutions for 3 days.

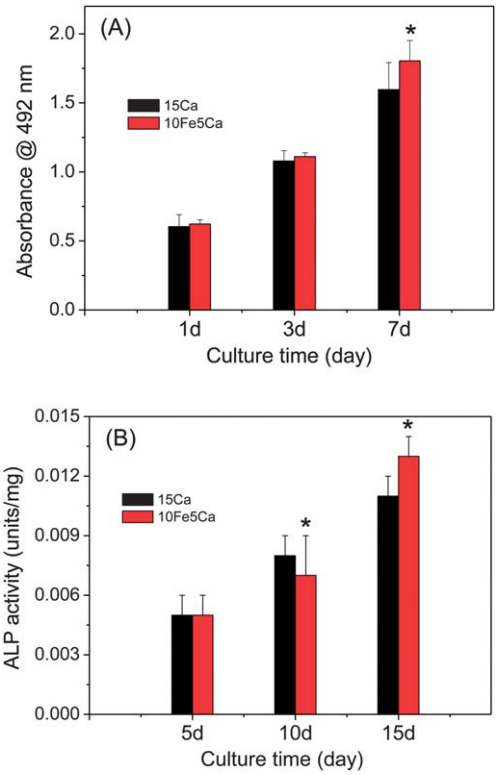

Fig. 9 The proliferation (A) and ALP activity (B) of MC3T3-E1 cells on the 15Ca and 10Fe5Ca MBG scaffolds.

Proliferation and differentiation of osteoblast cells on magnetic MBG scaffolds

It has been well understood that the proliferation and differentiation of osteoblast cells are the important steps that occur before bone mineralization, and the fundamental process of cell proliferation, differentiation and its function are governed by the interaction of cells with their substrate.[51,52] To further investigate the *in vitro* bioactivity of the magnetic MBG scaffolds, the proliferation, ALP activity and osteogenic expression of osteoblast-like cells, MC3T3-E1, on the magnetic MBG scaffolds were investigated in this study.

The proliferation and ALP activity of MC3T3-E1 cells on the 10Fe5Ca and 15Ca MBG scaffolds are shown in Fig. 9. It can be seen that proliferation of MC3T3-E1 cells had no obvious difference at 1 day. However with the increase of culture time, the 10Fe5Ca MBG scaffolds showed an increased cell proliferation compared to the 15Ca MBG scaffolds. On the other hand, compared to the 15Ca MBG scaffolds, the 10Fe5Ca MBG scaffolds exhibited a comparable ALP activity at 5 days, a little lower ALP activity at 10 days, but a higher ALP activity at 15 days. It suggested that the substitution of Fe_3O_4 for CaO in the MBG scaffolds could enhance the proliferation and ALP activity of MC3T3-E1 cells.

Cell differentiation was further evaluated by osteogenic expression determined by the expressions of osterogenic markers Colla1, Bglap2 and Ifitm5 at 5, 10 and 15 days of seeding MC3T3-E1 cells on the 10Fe5Ca and 15Ca MBG scaffolds. As shown in Fig. 10, Collagen type I mRNA expressions were upregulated on both MBG scaffolds, and the 10Fe5Ca MBG scaffolds regulated higher expression levels compared to the 15Ca MBG scaffolds. For Bglap2 and Ifitm mRNA expressions, the expression levels of both MBG scaffolds were close to each other at 5 days, and increased with increasing culture time. At 15 days, the expression levels of the 10Fe5Ca MBG scaffolds were much higher than those of the 15Ca MBG scaffolds. Therefore, the results of osteogenic expression indicated that the 10Fe5Ca MBG scaffolds were superior to the 15Ca MBG scaffolds in supporting MC3T3-E1 cell differentiation.

Several recent studies reported that the introduction of magnetic nanoparticles to biomaterials, such as CaP bioceramics and HA–PLA composite films, could promote bone formation and growth *in vitro* and *in vivo*.[53–55] In this study, the substitution of Fe_3O_4 for CaO in the MBG scaffolds did not change the 3D interconnected macroporous structure associated with mesoporous pore walls. However, the magnetic Fe_3O_4 component was incorporated in the 10Fe5Ca MBG scaffolds, which could play an important role in the enhancement of the proliferation and differentiation of osteoblast cells. On the other hand, previous studies demonstrated that the ionic environment including chemical composition and pH value, caused by the dissolution of ions from the biomaterials, could affect the biological response of cells.[37,56,57] In this study, the dissolution rates of Si ions from the 10Fe5Ca and 15Ca MBG scaffolds were similar, but the 10Fe5Ca MBG scaffolds exhibited

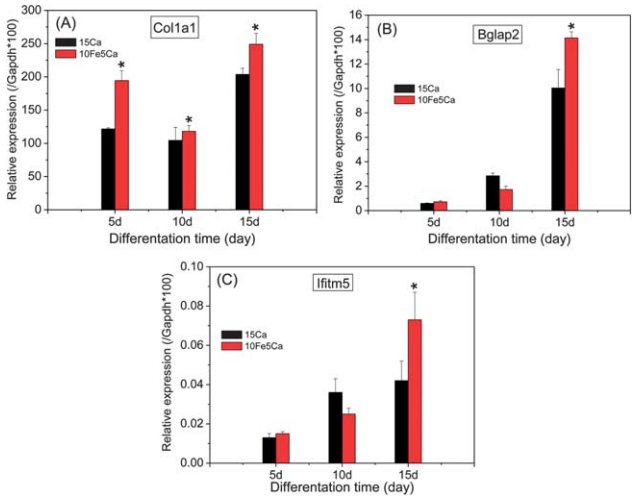

Fig. 10 Osteogenic expressions of Colla1 (A), Bglap2 (B) and Ifitm5 (C) of MC3T3-E1 cells on the 15Ca and 10Fe5Ca MBG scaffolds by quantitative RT-PCR analysis after 5, 10 and 15 days' culture.

a little lower Ca ion dissolution rate, resulting in more significant potential to stabilize the pH value in the surrounding environment compared to the 15Ca MBG scaffolds. Therefore, the beneficial pH environment may also be another important factor to facilitate cell proliferation and differentiation, and regulate the gene expression on the 10Fe5Ca MBG scaffolds.

Drug release from magnetic MBG scaffolds

To investigate the drug release property of the magnetic MBG scaffolds, gentamicin was used as a model drug for loading and release kinetics of the magnetic MBG scaffolds. Gentamicin loading efficiencies (mass of gentamicin/mass of scaffolds) of the 10Fe5Ca and 15Ca MBG scaffolds were close to each other, and estimated to be 10.9% and 12.1%, respectively. The accumulative gentamicin release from the 10Fe5Ca and 15Ca MBG scaffolds in SBF at 37 °C is shown in Fig. 11. Both MBG scaffolds exhibited a similar sustained release behavior during the whole period, and an initial fast release followed by a relatively slow release. It is similar to that reported in sustained drug release systems based on mesoporous silica due to the presence of mesoporous channels.[58] However, the release rate from the 10Fe5Ca MBG scaffolds was a little faster than that from the 15Ca MBG scaffolds, which might be attributed to a little pH difference of SBF solutions during gentamicin release. The adsorption of gentamicin molecules on the MBG scaffolds is determined by the hydrogen bonding, resulting in the easy desorption of gentamicin at the lower pH environment. As mentioned above, the 10Fe5Ca MBG scaffolds could induce SBF solution to a little lower pH value for soaking for the same period as the 15Ca MBG scaffolds. Xia *et al.* have also concluded that gentamicin release rate from the $CaO–SiO_2–P_2O_5$ MBG particles increased with the decrease of pH values of the release medium.[29] Therefore, the 10Fe5Ca MBG scaffolds have potential as a local sustained drug delivery system for bone regeneration.

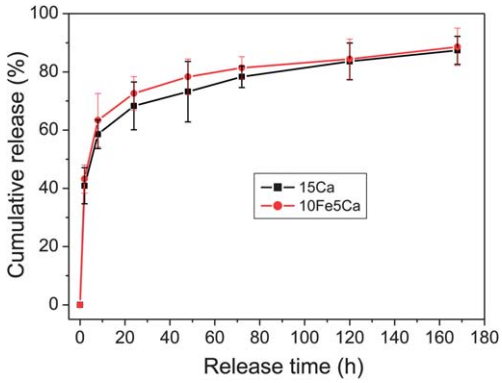

Fig. 11 Gentamicin release profiles from the 15Ca and 10Fe5Ca MBG scaffolds.

Conclusions

Magnetic 10Fe5Ca MBG scaffolds ($Fe_3O_4–CaO–SiO_2–P_2O_5$) with hierarchically mesoporous–macroporous structure and multifunctionality have been successfully prepared. Compared to the 15Ca MBG scaffolds, the 10Fe5Ca MBG scaffolds had similar interconnected macroporous network and mesoporous pore walls, but enhanced the physicochemical and biological properties to some extent. Due to the substitution of Fe_3O_4 for CaO in the MBG scaffolds, the 10Fe5Ca MBG scaffolds exhibited a slower ion dissolution rate and greater significant potential to stabilize the pH environment, facilitating osteoblast cell proliferation and differentiation. The 10Fe5Ca MBG scaffolds showed a good apatite-forming ability and a sustained drug release property similar to the 15Ca MBG scaffolds. Importantly, the 10Fe5Ca MBG scaffolds were superparamagnetic, and could generate heat under an alternating magnetic field for the potential application in hyperthermia therapy. Therefore, the magnetic 10Fe5Ca MBG scaffolds have potential for the regeneration of the critical-size bone defects caused by bone tumors by a combination of magnetic hyperthermia and local drug delivery therapy.

Acknowledgements

The authors gratefully acknowledge the support by the Program for Professor of Special Appointment (Eastern Scholar) at Shanghai Institutions of Higher Learning, National Natural Science Foundation of China (no. 51102166) and Shanghai Pujiang Program (no. 11PJ1407300), Innovation Program of Shanghai Municipal Education Commission (no. 12ZZ140) and Key Project of Chinese Ministry of Education (no. 212055).

References

1 B. B. Chen, *J. Clin. Rehabil. Tissue Eng. Res.*, 2011, **15**(16), 2973–2976.
2 G. M. Calori, E. Mazza, M. Colombo and C. Ripamonti, *Injury*, 2011, **42**(suppl. 2), S56–S63.
3 J. R. Jones and L. L. Hench, *J. Biomed. Mater. Res., Part B*, 2004, **68**, 36–44.
4 M. B. Coelho and M. M. Pereira, *J. Biomed. Mater. Res., Part B*, 2005, **75**, 451–456.

5 L. F. Tse, K. C. Wong, S. M. Kumta, L. Huang, T. C. Chow and J. F. Griffith, *Bone*, 2008, **42**, 68–73.
6 D. Arcos, R. P. Del Real and M. Vallet-Regi, *J. Biomed. Mater. Res., Part A*, 2003, **65**, 71–78.
7 F. M. Martín-Saavedra, E. Ruíz-Hernández, A. Boré, D. Arcos, M. Vallet-Regí and N. Vilaboa, *Acta Biomater.*, 2010, **6**, 4522–4531.
8 N. Bock, A. Riminucci, C. Dionigi, A. Tampieri, E. Landi, V. A. Goranov, M. Marcacci and V. Dediu, *Acta Biomater.*, 2010, **6**, 786–796.
9 G. Li, S. Feng and D. Zhou, *J. Mater. Sci.: Mater. Med.*, 2011, **22**, 2197–2206.
10 S. Panseri, C. Cunha, T. D'Alessandro, M. Sandri, A. Russo, G. Giavaresi, M. Marcacci, C. T. Hung and A. Tampier, *PLoS One*, 2012, **7**(6), e38710.
11 X. B. Zeng, H. Hu, L. Q. Xie, F. Lan, W. Jiang, Y. Wu and Z. W. Gu, *Int. J. Nanomed.*, 2012, **7**, 3365–3378.
12 S. Murakami, T. Hosono, B. Jeyadevan, M. Kamitakahara and K. Ioku, *J. Ceram. Soc. Jpn.*, 2008, **116**, 950–954.
13 M. Kawashita, K. Kawamura and Z. Li, *Acta Biomater.*, 2010, **6**, 3187–3192.
14 M. Banobre-Lopez, Y. Pineiro-Redondo, R. De Santis, A. Gloria, L. Ambrosio, A. Tampieri, V. Dediu and J. Rivas, *J. Appl. Phys.*, 2011, **109**, 07B313.
15 R. K. Singh, A. Srinivasan and G. P. Kothiyal, *J. Mater. Sci.: Mater. Med.*, 2009, **20**(S1), 147–S151.
16 C. S. S. R. Kumar and F. Mohammad, *Adv. Drug Delivery Rev.*, 2011, **63**, 789–808.
17 K. Kunieda, T. Seki, S. Nakatani, M. Wakabayashi, T. Shiro, K. Inoue, M. Sougawa, R. Kimura and K. Harada, *Br. J. Cancer*, 1993, **67**, 668–673.
18 S. P. Pathi, D. D. W. Lin, J. R. Dorvee, L. A. Estroff and C. Fischbach, *Biomaterials*, 2011, **32**, 5112–5122.
19 E. Verron, I. Khairoun, J. Guicheux and J.-M. Bouler, *Drug Discovery Today*, 2010, **15**, 547–552.
20 X. Yan, C. Yu, X. Zhou, J. Tang and D. Zhao, *Angew. Chem., Int. Ed.*, 2004, **43**, 5980–5984.
21 X. Yan, X. Huang, C. Yu, H. Deng, Y. Wang, Z. Zhang, S. Qiao, G. Q. Lu and D. Zhao, *Biomaterials*, 2006, **27**, 3396–3403.
22 A. López-Noriega, D. Acros, I. Izquierdo-Barba, Y. Sakamoto, O. Terasaki and M. Vallet-Regí, *Chem. Mater.*, 2006, **18**, 3137–3144.
23 Y. Zhu, C. Wu, Y. Ramaswamy, E. Kockrick, P. Simon, S. Kaskel and H. Zreiqat, *Microporous Mesoporous Mater.*, 2008, **112**, 494–503.
24 Y. Zhu and S. Kaskel, *Microporous Mesoporous Mater.*, 2009, **118**, 176–182.
25 A. Garcia, M. Cicuendez, I. Izquierdo-Barba, D. Arcos and M. Vallet-Regí, *Chem. Mater.*, 2009, **21**, 5474–5484.
26 D. Arcos, A. López-Noriega, E. Ruiz-Hernandez, O. Terasaki and M. Vallet-Regi, *Chem. Mater.*, 2009, **21**, 1000–1009.
27 X. Li, X. P. Wang, Z. L. Hua and J. L. Shi, *Acta Mater.*, 2008, **56**, 3260–3265.
28 M. Alcaide, P. Portolés, A. López-Noriega, D. Arcos, M. Vallet-Regí and M. T. Portolés, *Acta Biomater.*, 2010, **6**, 892–899.
29 W. Xia and J. Chang, *J. Controlled Release*, 2006, **110**, 522–530.
30 L. Zhao, X. Yan, X. Zhou, L. Zhou, H. Wang, J. Tang and C. Yu, *Microporous Mesoporous Mater.*, 2008, **109**, 210–215.
31 A. López-Noriega, D. Arcos and M. Vallet-Regí, *Chem.–Eur. J.*, 2010, **16**, 10879–10886.
32 Y. Zhu, X. Li, J. Yang, S. Wang, H. Gao and N. Hanagata, *J. Mater. Chem.*, 2011, **21**, 9208–9218.
33 Y. Zhu, Y. Zhang, C. Wu, Y. Fang, J. Yang and S. Wang, *Microporous Mesoporous Mater.*, 2011, **143**, 311–319.
34 C. Wu, Y. Zhou, W. Fan, P. Han, J. Chang, J. Yuan, M. Zhang and Y. Xiao, *Biomaterials*, 2011, **33**, 2076–2085.
35 C. Wu, R. Miron, A. Sculean, S. Kaskel, T. Doert, R. Schulze and Y. Zhang, *Biomaterials*, 2011, **32**, 7068–7078.
36 C. Wu, Y. Zhou, C. Lin, J. Chang and Y. Xiao, *Acta Biomater.*, 2012, **8**, 3805–3815.
37 A. J. Salinas, S. Shruti, G. Malavasi, L. Menabue and M. Vallet-Regi, *Acta Biomater.*, 2011, **7**, 3452–3458.
38 C. Wu, W. Fan, Y. Zhang, M. Gelinsky, J. Chang, G. Cuniberti, V. Albrecht, T. Friis and Y. Xiao, *Acta Biomater.*, 2011, **7**, 3563–3572.
39 T. Kokubo and H. Takadama, *Biomaterials*, 2006, **27**, 2907–2915.
40 S. Y. Ni, J. Chang and J. Chou, *J. Biomed. Mater. Res., Part A*, 2006, **76**, 196–205.
41 H. W. Kim, J. C. Knowles and H. E. Kim, *J. Mater. Sci.: Mater. Med.*, 2005, **16**, 189–195.
42 C. Wu, J. Chang, W. Zhai and S. Ni, *J. Mater. Sci.: Mater. Med.*, 2007, **18**, 857–864.
43 H. Yun, S. Kim and Y. Hyeon, *Chem. Commun.*, 2007, 2139–2141.
44 H. Yun, S. Kim, Y. Hyun, S. Heo and J. Shin, *J. Biomed. Mater. Res., Part B*, 2008, **87**, 374–380.
45 X. Li, X. Wang, H. Chen, P. Jiang, X. Dong and J. Shi, *Chem. Mater.*, 2007, **19**, 4322–4326.
46 P. Sepulveda, J. R. Jones and L. L. Hench, *J. Biomed. Mater. Res., Part A*, 2002, **59**, 340–348.
47 H. Zreiqat, Y. Ramaswamy, C. Wu, A. Paschalidis, Z. Lu, B. James, O. Birke, M. McDonald, D. Little and C. R. Dunstan, *Biomaterials*, 2010, **31**, 3175–3184.
48 Y. F. Chou, W. Huang, J. C. Dunn, T. A. Miller and B. M. Wu, *Biomaterials*, 2005, **26**, 285–295.
49 L. L. Hench and J. Wilson, *Science*, 1984, **226**, 630–636.
50 M. Cerruti and N. Sahai, *Rev. Mineral. Geochem.*, 2006, **64**, 283–313.
51 J. Beresford, S. Graves and C. Smoothy, *Am. J. Med. Genet.*, 1993, **45**, 163–178.
52 Y. Ramaswamy, C. Wu, H. Zhou and H. Zreiqat, *Acta Biomater.*, 2008, **4**, 1487–1497.
53 J. Meng, Y. Zhang, X. Qi, H. Kong, C. Wang, Z. Xu, S. Xie, N. Gu and H. Xu, *Nanoscale*, 2010, **2**, 2565–2569.
54 Y. Wu, W. Jiang, X. Wen, B. He, X. Zeng, G. Wang and Z. Gu, *J. Biomed. Mater. Res.*, 2010, **5**, 015001 (7pp).
55 A. J. Parsons, M. Evans, C. D. Rudd and C. A. Scotchford, *J. Biomed. Mater. Res., Part A*, 2004, **71**, 283–291.
56 P. Valerio, M. M. Pereira, A. M. Goes and M. F. Leite, *Biomaterials*, 2004, **25**, 2941–2948.
57 I. A. Silver, J. Deas and M. Erecinska, *Biomaterials*, 2001, **22**, 175–185.
58 M. Vallet-Regí, A. Rámila, R. P. del Real and J. Pérez-Pariente, *Chem. Mater.*, 2001, **13**, 308–311.

